RSC Advances

PAPER

View Article Online
View Journal | View Issue



Cite this: *RSC Adv.*, 2026, **16**, 21791

# Composites based on poly(*o*-toluidine) and reduced graphene oxide: from synthesis to optical characterization and potential applications in the energy storage field

T. Burlanescu,[ab] M. Vaduva,[b] A. Androne,[b] M. Paraschiv,[b] M. Cercel,[b] C. Negrila[b] and M. Baibarac *[b]

Three methods were used to prepare poly(*ortho*-toluidine)/reduced graphene oxide (POT/RGO) composites: (i) the interaction of the two constituents in the solid state, (ii) the chemical polymerization of *ortho*-toluidine (OT) in the presence of the RGO sheets, and (iii) the electrochemical polymerization of OT in the presence of the RGO sheets. Combining the results of Raman scattering, FTIR spectroscopy, and X-ray photoelectron spectroscopy, we demonstrated the following: (i) the interaction of POT with RGO in the solid state leads to the non-covalent functionalization of RGO with POT; (ii) the chemical polymerization of OT in the presence of RGO results in the covalent functionalization of RGO with POT in emeraldine base (EB) and leucoemeraldine salt (LS) and (iii) the electrochemical polymerization of OT assisted by RGO sheets leads to the covalent functionalization of RGO with POT-LS and POT-emeraldine salt (ES). The cyclic voltammetry (CV) studies indicated that the values for the voltammetric output currents of the POT/RGO composites are superior to those reported for POT. Electrochemical studies demonstrated a (a) battery-type behavior in the case of the electrodes based on POT-ES and POT/RGO composites prepared by chemical and electrochemical polymerizations and a (b) pseudocapacitive behavior for the electrodes based on POT-EB and composites prepared by the interaction of POT-EB with RGO in the solid state. High capacitance values of up to 1197.23 and 1524.62 mF $cm^{-2}$ were obtained for the symmetrical supercapacitors based on the electrodes containing the POT/RGO composites prepared by chemical and electrochemical polymerization, respectively, of OT in the presence of RGO sheets.

Received 11th January 2026
Accepted 8th April 2026

DOI: 10.1039/d6ra00288a

rsc.li/rsc-advances



## 1 Introduction

Conductive polymers, such polyaniline and polyaniline derivatives were among the first macromolecular compounds to attract attention for applications in electrochemical supercapacitors as early as 1984,[1] they being followed by those containing polypyrrole.[2] The main advantages of conducting polymers that enable their use in the field of supercapacitors are high specific capacitance, tunable electrical conductivity, manufacturing methods that do not require sophisticated equipment, and high flexibility.[3] The selection of suitable dopant acids in the case of PANI can be a key strategy for improving the electrochemical performance of electrodes based on them.[4]

The main advantages of carbon nanostructures, such as carbon nanotubes, carbon quantum dots, graphene, graphene oxide, and reduced graphene oxide (RGO), for their use in supercapacitors, are their large specific surface area, high electrical conductivity, high electrochemical stability, and eco-friendliness.[3] Considering these advantages, sustained efforts have been made to synthesize composites based on polyaniline (PANI) and graphene for use in supercapacitor applications.[5,6] Composites based on PANI and reduced graphene oxide (RGO) have been prepared by a number of methods, the most widely used being (a) the oxidative polymerization of aniline (ANI) in the presence of graphene oxide (GO)[5,7] or RGO[8] using ammonium persulphate (APS),[5,7,9] hydrogen peroxide ($H_2O_2$)[10] or ferric chloride ($FeCl_3$)[11] as oxidants in acidic conditions and (b) the electrochemical polymerization of ANI in the presence of RGO or GO, in the last case being followed by a reduction process.[12] Depending on the type of acid used in the polymerization reaction environment of ANI (0.2 M) (*e.g.* $H_2SO_4$ (0.1 M) or acetic acid (0.4 M)) in the presence of ammonium persulphate (0.25 M), conductivity values of the non-protonated form of PANI have been reported between $7.9 \times 10^{-9}$ S $cm^{-1}$ and $6 \times 10^{-8}$ S $cm^{-1}$, while the conductivity of the protonated form

[a]*University of Bucharest, Faculty of Physics, Atomistilor Street 405, Magurele, Romania*
[b]*National Institute of Materials Physics, Atomistilor Street 405A, Magurele, Romania. E-mail: barac@infim.ro*

varies between 0.036 and 3.7 S $cm^{-1}$.[13] PANI shows (a) three non-protonated forms, namely, leucoemeraldine base, emeraldine base, and pernigraniline base, which are differentiated by the proportion of oxidized and reduced entities from the macromolecular chain[14] and (b) three protonated forms, namely, leucoemeraldine salt, emeraldine salt, and pernigraniline salt.[14] The protonated structure of the PANI-salt can be obtained by (a) the protonic acid doping process of the three forms of PANI-base; (b) the pseudo-protonic acid doping process of PANI-EB, and (c) the redox doping process.[15] These forms are also in the chemical structure of the PANI derivatives, such as poly(*o*-toluidine) (POT).

Poly(*o*-anisidine) and POT are polyaniline derivatives that are used in the preparation of graphene-containing composite materials.[16] The chemical polymerization of *o*-anisidine and *o*-toluidine (OT) monomers in an acidic medium in the presence of graphene, ammonium peroxodisulfate ($(NH_4)_2S_2O_8$), and HCl results in composites containing poly(*o*-anisidine)-emeraldine salt or poly(*o*-toluidine)-emeraldine salt and graphene [16] The energy densities of supercapacitors obtained when composites of the PANI/graphene, poly(*o*-anisidine)/graphene, and POT/graphene types were used as electrode materials were reported to be 52.8 Wh $kg^{-1}$, 38.3 Wh $kg^{-1}$, and 59.26 Wh $kg^{-1}$, respectively.[16] However, despite numerous studies on PANI-based composites with graphene derivatives, a clear correlation between the synthesis method, type of functionalization (covalent *versus* non-covalent), structural characteristics, and electrochemical performance is still lacking for the POT/RGO composite-based systems. This limits the rational design of such composites for high-performance supercapacitor applications. This work provides, for the first time, a comparative analysis of three synthesis strategies leading to distinct bonding configurations between POT and RGO, and correlates these structural differences with their electrochemical performance. The adopted strategies for the synthesis of POT and RGO-based composites include the following: (a) the interaction of the two constituents in the solid state, *i.e.*, POT and RGO; (b) the chemical polymerization of the OT monomer in the presence of $K_2Cr_2O_7$, $H_2SO_4$, and RGO; and (c) the electrochemical polymerization of OT in the presence of $H_2SO_4$ and RGO. The novelty of this study lies in the comparative analysis of these methods in terms of the type of interaction established between POT and RGO, as well as in establishing correlations between structural features (evidenced by spectroscopic techniques) and electrochemical performance. By clarifying how the synthesis route governs the functionalization mechanism and the resulting capacitive properties, this work contributes to a better understanding and optimization of conducting polymer/graphene-based electrode materials for supercapacitors.

## 2 Experiments

The following materials were used in this work: OT, $H_2SO_4$, dimethylformamide (DMF), $K_2Cr_2O_7$, $NH_4OH$, $CH_3CN$, graphite flakes, $H_2O_2$, $C_2H_5OH$, poly(vinylidene fluoride) (PVDF), Nafion membranes, diethyl ether, dibutyl phthalate (DBP), acetone, and $KMnO_4$, all of which were purchased from Sigma-Aldrich.

### 2.1 Synthesis of RGO and the POT/RGO composites

**2.1.1 Synthesis of RGO.** RGO was obtained by reducing graphene oxide (GO) using Marcano's method[17] in the presence of hydrazine. Briefly, the method involved the interaction of 3 g of graphite flakes with a mixture of concentrated acids in a volumetric ratio of 9 : 1, *i.e.*, 360 mL $H_2SO_4$ and 40 mL $H_3PO_4$, to which were added 18 g of $KmnO_4$. Adding $KmnO_4$ causes the release of energy in the form of heat, which contributes to raising the temperature of the reaction mixture up to 80 °C. The temperature of the reaction mixture was lowered to room temperature by using an ice bath and remained under magnetic stirring for 12 hours, after which 3 mL of $H_2O_2$ with a concentration of 30 wt% was added. Subsequently, the mixture was centrifuged (4000 rpm for 4 hours) and the solid material was washed with 200 mL of deionized water, 200 mL of 30% HCl, 200 mL of $C_2H_5OH$, and coagulated with 300 mL of ether, then centrifuged once more at 4000 rpm for 4 hours. The solid material was redispersed in water and then filtered under vacuum, and then the solid product was dried to constant mass, resulting in 5.8 g of GO being obtained. Subsequently, GO was reduced with 5 mL hydrazine hydrate, resulting in RGO.

**2.1.2 Synthesis of POT.** The chemical polymerization of OT in the presence of $K_2Cr_2O_7$ and $H_2SO_4$ was carried out according to ref. 18.

**2.1.3 Synthesis of the POT/RGO composites.** To prepare the POT-EB/RGO composite, the chemical polymerization of POT-EB was conducted as described above; the only difference was the addition of 0.1 g and 0.01 g RGO, respectively, in the 0.18 M OT in 50 mL of 2 M $H_2SO_4$, which was allowed to interact with a solution of 0.05 M $K_2Cr_2O_7$ in 50 mL of 2 M $H_2SO_4$. The polymerization time was 2 hours, during which a dark green precipitate, corresponding to the POT-ES/RGO composite, was obtained. After filtration of the reaction mixture, the POT-ES/RGO composite was allowed to interact with a 1 M $NH_4OH$ solution, 500 mL of distilled water, and 100 mL of $CH_3CN$ to remove the oligomers from the reaction product, and then dried at room temperature for 24 h to a constant mass. The final compound corresponds to the POT-EB/RGO composites with RGO concentrations of 20 wt% and 10 wt%, respectively. The color of the powders of the POT-EB/RGO composites was dark blue.

Another chemical method used to obtain POT-EB/RGO and POT-ES/RGO composites was the solid-state interaction of the two constituents through grinding, resulting in composites in which the RGO concentrations were 25 wt% and 50 wt%.

Electrochemical polymerization is an alternative method for obtaining POT-ES and its POT-ES/RGO composite. For the electrochemical synthesis of POT-ES, a semi-aqueous solution of 0.1 M OT in 0.5 M $H_2SO_4$ was used, with the volumetric ratio of $H_2O$ : DMF being 1 : 1.[18] The electrosynthesis of the POT/RGO composite involves the preparation of the following: (i) a solution of RGO in DMF (50 mL, 0.1 mg $mL^{-1}$), dispersion of RGO into DMF taking place by ultrasonication for 15 min; and (ii) an aqueous solution of 0.1 M OT in 0.5 M $H_2SO_4$ (50 mL). Subsequently, the two solutions were mixed and homogenized by ultrasonication for 5 min. The reaction mixture was introduced

into a single-compartment cell, which was accessorized with three electrodes as follows: a Pt working electrode with an area of 1 $cm^2$, an auxiliary electrode made of Pt, and an Ag/AgCl reference electrode. Using CV, the potential range used was between −200 and +900 mV *vs.* Ag/AgCl, with the potential scanning speed in both cases being 50 mV $s^{-1}$.

### 2.2 Preparation of electrodes for supercapacitor cells

In the case of POT/RGO samples obtained by chemical interaction of the two constituents or by chemical polymerization of OT in the presence of RGO, the resulting composites were used as such in the preparation process of electrodes for supercapacitor cells. In the case of POT-ES/RGO samples obtained electrochemically, after drying the electrodes, the films were scraped from the surface of the working electrode, and then used in the preparation of electrodes for supercapacitor cells according to the protocol presented below.[19] The electrodes were prepared by mixing and stirring 80 wt% of active material, *i.e.*, POT and the POT/RGO composites, 15 wt% of super-P conductive carbon black, 5 wt% of PVDF in the role of binding agent, 2 drops of DBP, and 1 mL of acetone. After 12 hours of mixing under magnetic stirring, a homogeneous paste was obtained. The paste was poured onto a glass surface, and after acetone evaporation, the resulting film was detached and washed with diethyl ether to remove DBP. The resulting film was cut into several circles with a diameter of 8 mm, which were used as electrodes in the supercapacitor cells.

### 2.3 Assembly of supercapacitor cells

The electrodes were assembled in Swagelok cells from stainless steel and were composed of two current collectors and a spring compression system.[19] The electrolyte used in the supercapacitor cells corresponds to a commercial Nafion 117 membrane that was activated with 1 M $H_2SO_4$ solution.[20] The assembly of Swagelok-type cells was carried out by successively inserting the electrochemical components into a cylindrical metallic housing, internally insulated with a thin PET foil to prevent short circuits, according to ref. 21. According to the schemes presented in ref. 19 and 21, the assembly was performed in a layered configuration, in the following order: current collector, anode, Nafion membrane activated with $H_2SO_4$, cathode, current collector, followed by the helical compression spring, which provides the internal pressure necessary to maintain mechanical contact between the layers of the cell. To ensure a constant and reproducible pressure on the electrode stack, the cell was assembled under a torque of 1.2 N m using a calibrated torque wrench. The Swagelok-type cell was sealed through its threaded stainless-steel body and fittings, which ensure mechanical compression and tight sealing of the internal components. This design prevents exposure to air and moisture during operation. The Swagelok-type cell is sealed through its threaded stainless steel body and fittings, which ensure mechanical compression and tight sealing of the internal components. This design prevents exposure to air and moisture during operation.

The assessment of the electrochemical properties of the POT/RGO composites as electrode materials for the supercapacitors was carried out by CV.

Fig. S1 shows a schematic flowchart summarizing the synthesis routes of RGO and the POT/RGO composites, the electrode preparation, and cell assembly.

### 2.4 Optical and electrochemical characterizations of composite materials

The Raman spectra of the compounds analyzed in this work were recorded at the excitation wavelength of 1064 nm using a MultiRam FTRaman spectrophotometer from Bruker.

The IR spectra of the compounds analyzed in this work were recorded with the FTIR spectrophotometer, model Vertex 80, from Bruker, in the transmission geometry in the case of chemically prepared compounds. POT-ES or its composites were electrochemically synthesized on the Pt electrode; the attenuated total reflection (ATR) geometry was used for recording FTIR spectra.

X-ray photoelectron spectroscopy (XPS) spectra were recorded using a SPECS spectrometer equipped with a Phoibos 150 electron energy analyzer. An aluminum anode (Al K$\alpha$ 1486.74 eV) was used as a monochromatic X-ray source. All studies were conducted under ultra-high vacuum conditions ($10^{-7}$ Pa). The obtained data were analyzed using the SDPv7.0 program.

A Voltalab 80 potentiostat/galvanostat, purchased from Radiometer Analytical, was used for electrochemical studies.

## 3 Results and discussion

### 3.1 Optical properties of the POT/RGO composites synthesized by the chemical polymerization method and the solid-state interaction

Fig. 1 and 2 show the Raman spectra of RGO, POT-EB, and POT-EB/RGO composites obtained by the interaction of the two

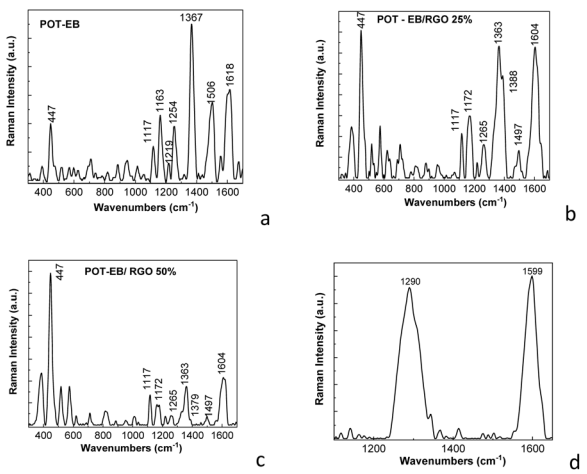


Fig. 1 Raman spectra of POT-EB (a), POT-EB chemically interacted with RGO, leading to the POT/RGO composites with a concentration of the RGO sheets equal to 25 wt% (b) and 50 wt% (c) respectively. Figure (d) shows the Raman spectrum of RGO.

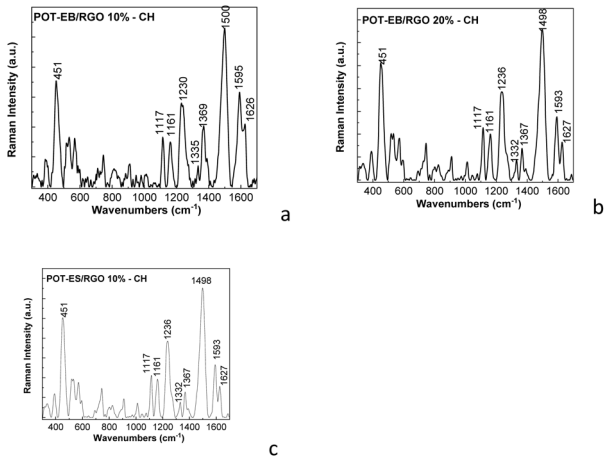


Fig. 2 Raman spectra of POT-EB/RGO composites, having RGO concentrations of 10 wt% (a) and 20 wt% (b), obtained by the chemical polymerization of OT in the presence of RGO. Figure (c) corresponds to the Raman spectrum of the POT-ES/RGO composite, with the concentration of RGO equal to 10 wt%, obtained by chemical polymerization of OT in the presence of RGO.

constituents and by chemical polymerization of OT in the presence of RGO.

The Raman spectrum of POT-EB (Fig. 1a) shows Raman lines at 447, 1117, 1163, 1219, 1254, 1367, 1506 and 1618 $cm^{-1}$, which are attributed, by similarity to those reported in the case of PANI-EB, to the following vibrational modes: deformation of the aromatic ring, deformation of the benzene (B) ring + C–H bending in the $CH_3$ group, C–H bending in the B ring, C–N stretching + C–C + C–H stretching in the B ring, C–C stretching in the B ring, C–C stretching in the quinoid ring (Q) + C–H bending in the B ring, C=N stretching and C–C bending + C–H stretching in the B ring.[22,23] RGO's Raman spectrum is characterized by two bands with maxima located at 1290 and 1599 $cm^{-1}$ (Fig. 1d), which have been assigned to the vibrational mode $E_{2g}$ at the centre of the Brillouin zone specific to $sp^3$-hybridized carbon atoms and radial vibrational modes of hexagonal carbon rings containing $sp^2$-hybridized carbon atoms.[24] Compared to the Raman spectrum of POT-EB, the following variations were observed in the Raman spectra of the POT-EB/RGO composites obtained by the interaction of the two constituents, when the concentration of RGO in the mass of the composite was equal to 20 wt% and 50 wt% (Fig. 1b and c): (i) an up-shift of the Raman line from 1254 $cm^{-1}$ (Fig. 1a) to 1265 $cm^{-1}$ (Fig. 1b and c); (ii) the Raman line localized in the spectral range 1300–1400 $cm^{-1}$ has the maximum at 1363 $cm^{-1}$ (Fig. 1b and c), its semi-width being greater as a result of the presence of a new component having the maximum at 1388 $cm^{-1}$ (Fig. 1b) and 1379 $cm^{-1}$ (Fig. 1c); (iii) a down-shift of the Raman lines from 1506 and 1618 $cm^{-1}$ (Fig. 1a) to 1497 and 1604 $cm^{-1}$ (Fig. 1b and c); (iv) the ratios of the intensities of the Raman lines with peaks at 447 $cm^{-1}$ and 1363–1367 $cm^{-1}$ ($I_{447}/I_{1363-1367}$) range from 0.36 (Fig. 1a) to 1.1 (Fig. 1b) and 3.9 (Fig. 1c). The increase in the relative intensity of the Raman line at 447 $cm^{-1}$, which induces the variation of the $I_{447}/I_{1363-1367}$ ratio from 0.36 to 3.9, indicates the appearance of steric hindrance effects, which can be explained as a consequence of a non-covalent functionality of the RGO sheets with POT-EB, when π–π* bonds are formed between the aromatic rings of the POT and the hexagonal carbon cycles of the RGO.

For composites synthesized *via* chemical polymerization, more pronounced changes were observed, as shown in Fig. 2. Thus, the Raman spectra of POT-EB/RGO composites synthesized by chemical polymerization of OT in the presence of RGO show the following variations compared to the Raman spectrum of POT-EB: (i) the Raman line from 447 $cm^{-1}$ (Fig. 1a) shifted to 451 $cm^{-1}$ (Fig. 2); the ratios of the intensities of the Raman lines situated at 451 and 1363 $cm^{-1}$ are equal to 1.73 (Fig. 2a), 3.7 (Fig. 2b) and 1.76 (Fig. 2c); (ii) the presence of a new Raman line at 1332–1335 $cm^{-1}$ (Fig. 2) indicates the presence of the protonated structure of POT-ES;[15] (iii) the shape of the Raman band situated in the spectral range 1550–1650 $cm^{-1}$ shows two components at 1593–1595 and 1626–1627 $cm^{-1}$ (Fig. 2), which were assigned to the vibrational modes of C–C stretching in the B ring + C=C stretching in the Q ring and C–C stretching in the B ring;[15] (iv) the Raman line from 1506 $cm^{-1}$ (Fig. 1a) is shifted to 1500 $cm^{-1}$ (Fig. 2a) and 1498 $cm^{-1}$ (Fig. 2b and c); (v) the ratios of the intensities of the Raman lines from 1498–1506 $cm^{-1}$ and 1618–1627 $cm^{-1}$ are 0.86 (Fig. 1a), 2.52 (Fig. 2a), 4.02 (Fig. 2b) and 2.55 (Fig. 2c). The changes in intensity ratios (*e.g.*, $I_{451}/I_{1363}$ and $I_{1498-1506}/I_{1618-1627}$) confirm a higher degree of structural reorganization and electronic delocalization compared to the solid-state composites. The Raman lines at 1332–1335, 1593–1595, and 1626–1627 $cm^{-1}$ confirm the formation of protonated POT-ES structures in the mass of composites (Fig. 2). This structural feature is particularly important for electrochemical applications, as protonation enhances charge delocalization along the polymer chains, thereby facilitating redox processes and improving capacitive performance.

The Raman spectra recorded on POT/RGO composites samples synthesized *via* chemical polymerization of OT in the presence of RGO reveal, among the lines specific to each component, evidence of a protonated POT-ES structure as a consequence of an extended charge delocalization. Therefore, in the following, additional information is provided, *via* FTIR spectroscopy, regarding the molecular structure of the composites, obtained from interactions in the solid state of the POT with RGO and chemical polymerization of OT in the presence of RGO (Fig. 3). The FTIR spectrum of POT-EB is characterized by IR bands with maxima at 444, 816, 879, 1005, 1111, 1155, 1242, 1306, 1491 and 1601 $cm^{-1}$, attributed to vibrational modes of B-ring deformation, out-of-plane deformation of the substituted B, deformation of the three-substituted B, the B deformation, deformation of the B ring + C–H bending in B, the C–H in-plane bending in Q, C–N stretching in the structure (B)–N=(Q), C–N stretching in the Q ring, C–C stretching + C–H + N–H and the N=(Q)=N structure, respectively.[23] The IR spectrum of POT-ES is characterized by IR bands with maxima at 438-560-617, 804, 874, 994, 1105, 1165, 1261, 1325, 1485 and 1595 $cm^{-1}$, which are assigned to vibrational modes of B deformation, out-of-plane deformation of the

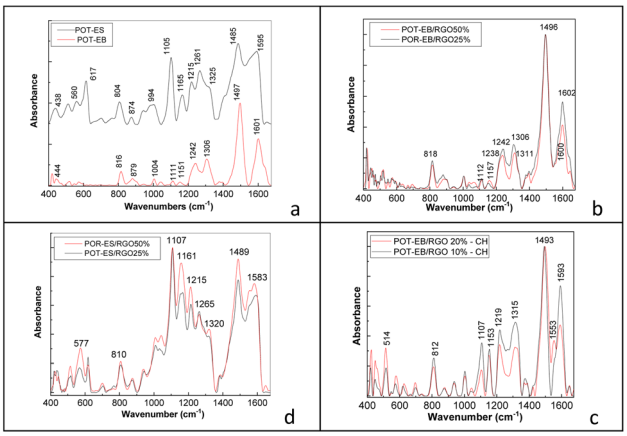


Fig. 3 IR spectra of (a) POT-EB (black curve) and POT-ES (red curve); (b) POT-EB/RGO composites obtained by the solid-state interaction of the two constituents (RGO concentration was equal to 25 wt% (black curve) and 50 wt% (red curve)): (c) POT-EB/RGO composites obtained by the chemical polymerization of OT in the presence of RGO, when the concentration of RGO in the mass of composites is 10 wt% (black curve) and 20 wt% (red curve); and (d) POT-ES/RGO composites, having RGO concentrations of 25 wt% (black curve) and 50 wt% (red curve), which were obtained by the interaction of the two constituents.

B-substituted ring, deformation of the three-substituted B ring, the B deformation, the B deformation + C–H bending in the B, the C–H bending in-plane in the Q ring, stretching the C–N bond in the (B)–$NH^+$=(Q) structure, C–N stretching in the Q ring, stretching the C–C + C–H + N–H bonds and the N=(Q)=N structure, respectively.[22,25]

A careful analysis of Fig. 3a highlights the following as main changes when POT-EB is transformed into POT-ES: (i) the down-shift of the IR band from to 1111 $cm^{-1}$ to 1105 $cm^{-1}$ simultaneously with the increase in the absorbance of the IR band at 1111 $cm^{-1}$; (ii) an up-shift of the IR band from 1306 $cm^{-1}$ to 1325 $cm^{-1}$; (iii) the down-shift of the IR bands from 1497 and 1601 $cm^{-1}$ to 1485 and 1595 $cm^{-1}$ simultaneously with the change in the ratio between the absorbance of these IR bands ($A_{1601-1595}/A_{1497-1485}$) from 0.57 to 0.94. These changes reflect the protonation process and modification of the electronic structure. Compared to the IR spectrum of POT-EB (Fig. 3a), the IR spectra of the POT-EB/RGO composites obtained by the interaction of the two constituents (Fig. 3b) show only the shift of the IR bands from 1151, 1242, and 1306 $cm^{-1}$ (Fig. 3a) to 1157, 1238, and 1311 $cm^{-1}$, respectively (Fig. 3b), confirming weak interactions between POT and RGO. Much more significant changes were observed in the case of the FTIR spectra of POT-EB/RGO composites synthesized by chemical polymerization of OT in the presence of RGO, as follows: (i) a down-shift of IR bands from 816, 1242, 1497 and 1601 $cm^{-1}$ (Fig. 3a) to 812, 1219, 1493 and 1593 $cm^{-1}$ (Fig. 3c); (ii) an increase in the absorbance of IR bands with maxima at 1107 and 1153 $cm^{-1}$ (Fig. 3c); (iii) an up-shift of the IR band from 1306 $cm^{-1}$ (Fig. 3a) to 1315 $cm^{-1}$ (Fig. 3c); (iv) ratio between the absorbance of IR bands with maxima at 1306–1315 and 1107–1111 $cm^{-1}$ ranges from 6 (Fig. 3a) to 1.88 and 1.39 in the case of POT-EB/RGO composites with a RGO concentration equal to 10 wt% and 20 wt%, respectively (Fig. 3c); (v) the ratio between the absorbance of IR bands from 1497–1493 and 1306–1315 $cm^{-1}$ ranges from 3.13 (Fig. 3a) to 3.09 and 2.03 for POT-EB/RGO composites with a RGO concentration of 10 wt% and 20 wt% respectively (Fig. 3c); (vi) the $A_{1593}/A_{1493}$ ratio is equal to 0.47 and 0.73 in the case of the composites with a RGO concentration equal to 10 wt% and 20 wt%, respectively (Fig. 3c). These variations indicate the presence of a protonated structure in the case of composites obtained by the chemical polymerization of OT in the presence of RGO sheets, which successively interacted with $NH_4OH$ solution. Fig. 3d shows the FTIR spectra of the POT-ES/RGO composites obtained by the interaction of the two constituents. Compared to the IR spectrum of POT-ES, in the case of IR spectra of POT-ES/RGO composites with RGO concentration in the composite mass of 25 wt% and 50 wt%, the following variations were observed: (a) an up-shift of IR bands from 804 and 1485 $cm^{-1}$ (Fig. 3a) to 810 and 1489 $cm^{-1}$ (Fig. 3d); (b) a down-shift of IR bands from 1325 and 1595 $cm^{-1}$ (Fig. 3a) to 1320 and 1583 $cm^{-1}$ (Fig. 3d); and (c) the change in the ratios between absorbances of IR bands at ($c_1$) 1106 and 1215 $cm^{-1}$, from 1.23 (red curve in Fig. 3a) to 1.37 (red curve in Fig. 3d) and 1.65 (black curve in Fig. 3d); ($c_2$) 1106 and 1265 $cm^{-1}$, from 1.1 (red curve in Fig. 3a) to 1.79 (red curve in Fig. 3d) and 1.89 (black curve in Fig. 3d); and ($c_3$) 1106 and 1489 $cm^{-1}$, from 0.89 (red curve in Fig. 3a) to 1.29 (red curve in Fig. 3d) and 1.08 (black curve in Fig. 3d). Taking into account the variations reported in Fig. 2 and 3, the reaction of chemical polymerization of OT in the presence of RGO can be written as follows in Scheme 1.

In our opinion, Scheme 1 can explain the presence of the Raman lines at 1332–1335, 1593–1595 and 1626–1627 $cm^{-1}$, and IR bands at 1311–1320 $cm^{-1}$, as well as the value of the $A_{1593}/A_{1493}$ ratio equal to 0.73 in the case of composites prepared by chemical polymerization of OT in the presence of RGO that were successively interacted with $NH_4OH$ solution. Additional results that support Scheme 1 were obtained *via* XPS spectroscopy. Fig. 4 shows XPS C 1s spectra of RGO, POT-EB, and the POT-EB/RGO composites obtained by the interaction of the two constituents and by chemical polymerization of OT in the presence of RGO.

Fig. 4a shows the deconvolution of the XPS C 1s spectrum of RGO, which reveals four bands with maxima located at 284.5,

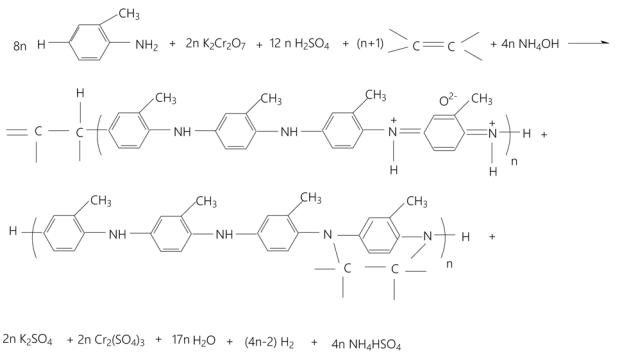


Scheme 1 Reaction of the chemical polymerization of OT in the presence of RGO.

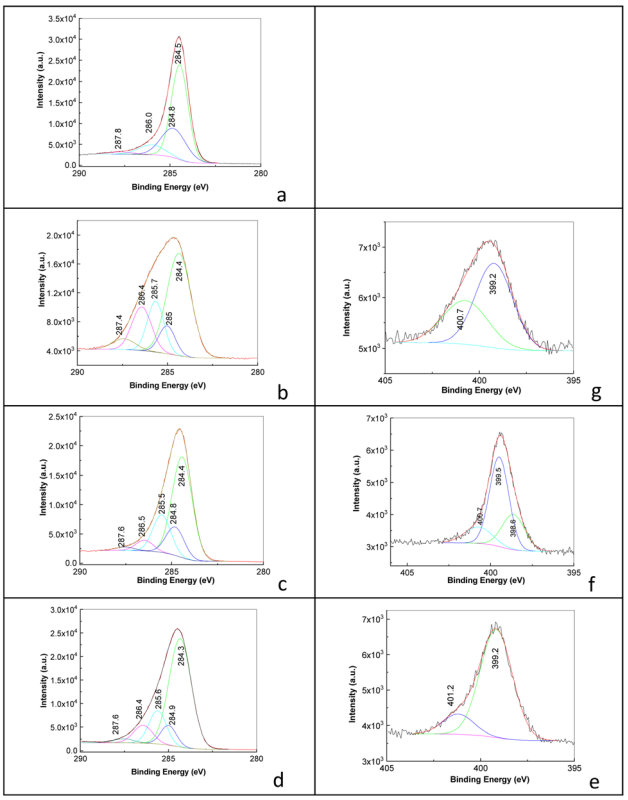


Fig. 4 The XPS C 1s spectra of RGO (a), the chemically synthesized POT-EB/RGO composites (with 10 wt% RGO) (b) and composites POT/RGO obtained through solid-state interaction with a content of 25 wt% RGO (c) and POT-EB (d); figures (e)–(g) show XPS N 1s spectra of the POT-EB and the POT-EB/RGO composite chemically polymerized with 10 wt% RGO and the POT-EB/RGO composite with 25% RGO obtained through solid-state interaction. Black and red curves correspond to experimental XPS spectra and the total fit of the XPS spectra deconvolution.

284.8, 286, and 287.8 eV, assigned to C=C bonds in aromatic rings, C–C and C–H, C–O in the epoxy/hydroxyl group, and C=O in the carbonyl group.[26] The deconvolution of the XPS C 1S spectrum of POT-EB (Fig. 4d) highlights five bands with maxima located at 284.3, 284.9, 285.6, 286.4, and 287.6 eV, which were assigned to bonds of the type C=C (C hybridized $sp^2$), C–C/C–H, C–N/C=N, C–O–H, and C=O.[27] The XPS N 1s spectrum of POT-EB (Fig. 4e) highlights two bands with maxima located at 399.2 and 401.2 eV, which were assigned to C–N=C and C–NH–C bonds.[28] In the case of POT-EB/RGO composites obtained by the interaction of the two constituents, (a) the XPS C 1s spectrum highlights five bands with maxima situated at 284.3, 284.9, 285.6, 286.4, and 287.6 eV (Fig. 4c); and (b) the XPS N 1s spectrum highlights two bands with maxima at 399.2 and 401.2 eV (Fig. 4g). In this case, the $I_{C-N}/I_{C=N}$ ratio is equal to 0.64. In the case of POT-EB/RGO composites obtained by chemical polymerization of OT in the presence of RGO, (a) the XPS C 1s spectrum highlights five bands with maxima located at 284.4, 285, 285.7, 286.4, and 287.4 eV (Fig. 4b); and (b) the XPS N 1s spectrum highlights two bands with maxima at 399.2 and 400.7 eV (Fig. 4f). A careful analysis of the ratio between intensities of the bands with maxima at 400.7–401.2 eV and 399.2 eV ($I_{C-N}/I_{C=N}$) indicates that its value is equal to 0.64 in the case of POT-EB and 0.89 when the POT-EB/RGO composite was obtained by chemical polymerization of OT in the presence of RGO. This result confirms that composites obtained by chemical polymerization of OT in the presence of RGO lead to a higher share of C–N bonds as a result of the above reaction. This suggests a stronger electronic interaction between the polymer chains and the RGO surface, likely involving partial charge transfer. For a better understanding of these results, it should be noted that the second reaction product of Scheme 1 can be written as follows:

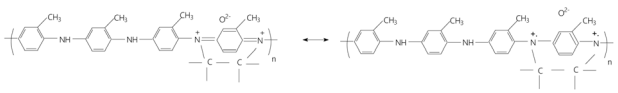

Summarizing all these, the spectroscopic results consistently indicate that the interaction mechanism between POT and RGO strongly depends on the synthesis route. In the case of composites obtained by the solid-state interaction, the presence of π–π stacking leads to steric hindrance and limited electronic delocalization. In contrast, chemical polymerization promotes partial protonation (POT-ES) and stronger electronic coupling between POT chains and RGO sheets, as evidenced by the Raman bands at 1332–1335 $cm^{-1}$ and the XPS increase in C–N bonds. In our opinion, these structural differences are expected to directly influence the electrochemical response as a consequence of enhanced conjugation and protonation, which facilitate charge transport, while stronger interfacial interactions with RGO improve electron mobility and ion accessibility during redox processes. In the case of solid-state composites, the predominance of π–π interactions and steric hindrance limits charge delocalization and electron transport across the interface. As a result, a lower electrochemical activity is expected. In contrast, chemical polymerization leads to the following: (i) partial protonation of the polymer (POT-ES), (ii) increased density of C–N bonds, and (iii) stronger electronic coupling with RGO sheets. These features enhance charge carrier mobility, facilitate redox processes, and improve ion accessibility within the composite structure. Consequently, these materials are expected to exhibit superior electrochemical performance, including higher current densities and capacitance values, as will be demonstrated in the following sections. Also, significant differences in electrochemical behavior are expected between the composites obtained in this section and those resulting from electrochemical polymerization, whose optical properties are detailed in the next section.

### 3.2 Optical properties of the POT/RGO composites prepared by cyclic voltammetry

Fig. 5 shows cyclic voltammograms recorded during chemical polymerization of OT in the absence (Fig. 5a) and in the presence of the RGO sheets (Fig. 5b).

In the case of OT electrochemical polymerization in the absence of RGO, the following characteristics of cyclic voltammograms were observed, as shown in Fig. 5a.

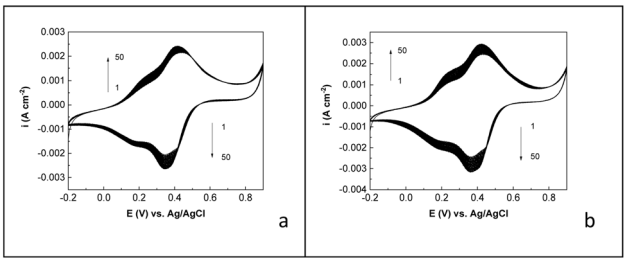


Fig. 5 Cyclic voltammograms recorded during the electrochemical polymerization of 0.1 M OT in a semi-aqueous solution of 0.5 M $H_2SO_4$ in the absence (a) and presence (b) of RGO sheets. The scan rate of the potential was 50 mV $s^{-1}$.

(a) In the case of the first cyclic voltammogram, during anodic scanning, the potential ranged from −200 to 900 mV; an oxidation peak was observed, with the anodic potential located at 436 mV, which was accompanied by another maximum with the potential at 238 mV; the current densities of the two oxidation peaks at 436 and 238 mV are equal to 2.1 mA $cm^{-2}$ and 0.8 mA $cm^{-2}$. During cathodic scanning of the potential, *i.e.*, from 900 mV to −200 mV, a reduction maximum characterized by a cathodic potential equal to 352 mV was observed, accompanied by another reduction maximum with a potential equal to 182 mV; the two reduction maxima at 352 and 182 mV are characterized by current densities equal to 2 mA $cm^{-2}$ and 1.5 mA $cm^{-2}$, respectively.

(b) In the case of the 50th cyclic voltammogram, it was observed that at the anodic scanning of the potential, *i.e.* from −200 to 900 mV, an oxidation maximum was observed with an anodic potential at 412 mV, accompanied by another maximum with the potential situated at 244 mV; the current densities of the two oxidation maxima having potentials at 412 and 244 mV are equal to 2.4 mA $cm^{-2}$ and 1.2 mA $cm^{-2}$. During cathodic scanning of the potential, *i.e.*, from 900 mV to −200 mV, a reduction maximum, characterized by a cathodic potential of 346 mV, was observed; this cathodic peak was accompanied by another peak with a potential of 182 mV. The two cathodic maxima at 346 and 182 mV are characterized by current densities of 2.6 mA $cm^{-2}$ and 1.7 mA $cm^{-2}$, respectively.

Regardless of the number of cyclic voltammograms recorded at the electrode/electrolyte interface, two oxidation–reduction processes were evidenced by the oxidation and reduction maxima with potentials located at (i) 436 mV and 352 mV as well as 238 mV and 180 mV, respectively, in the case of the first voltammogram and (ii) 412 mV and 346 mV as well as 244 mV and 180 mV, respectively, in the case of the 50th cyclic voltammogram. All these variations were accompanied by a gradual increase in the anode and cathode current densities. The potential difference is equal to the difference between the anode maximum potential ($E_a$) and cathode peak potential ($E_c$), which can be written as follows: $\Delta E = E_a - E_c$. Therefore, it follows that the two oxidation–reduction processes are characterized by $\Delta E$ equal to (i) 84 mV and 58 mV in the case of the first cyclic voltammogram, and (ii) 66 mV and 64 mV in the case of the 50th cyclic voltammogram. The ratio of the anode and cathode peak current densities ($i_a/i_c$) is equal to (i) 1.05 and 0.56 in the case of the first cyclic voltammogram, and (ii) 0.92 and 0.7 in the case of the 50th cyclic voltammogram. Generally speaking, a reversible process is characterized by $\Delta E = 56.5$ mV $n^{-1}$, where $n$ corresponds to the number of electrons involved in the oxidation/reduction processes, and a ratio of $i_a/i_c$ equal to 1. The results above indicate that the process of the electrochemical polymerization of OT on the Pt electrode is irreversible. At the end of the 50 cyclic voltammograms on the surface of the Pt electrode, the deposition of a green film corresponding to POT was observed.

When electrochemical polymerization of OT is carried out in the presence of RGO (Fig. 5b), a similar redox pattern is observed; however, several important differences can be identified as follows:

(a) In the case of the first cyclic voltammogram, during anodic scanning, an oxidation maximum with the anodic potential located at 430 mV is accompanied by another maximum at 246 mV; the current densities of the two oxidation maxima with anodic potentials at 430 and 246 mV are equal to 2.1 mA $cm^{-2}$ and 1.1 mA $cm^{-2}$. During cathodic scanning of the potential, a reduction maximum characterized by a cathodic potential of 364 mV was observed. This peak is accompanied by another cathodic maximum with the potential equal to 186 mV; the two reduction maxima with cathodic potentials at 364 and 186 mV are characterized by current densities equal to 2.4 mA $cm^{-2}$ and 1.6 mA $cm^{-2}$, respectively.

(b) In the case of the 50th cyclic voltammogram, at the anodic scanning of the potential, an oxidation maximum was observed with the anodic potential located at 420 mV, which was accompanied by another maximum with the potential at 244 mV; the current densities of the two oxidation maxima at 420 and 244 mV are equal to 2.9 mA $cm^{-2}$ and 1.6 mA $cm^{-2}$. During cathodic scanning of the potential, a reduction maximum characterized by a cathodic potential equal to 358 mV was observed, which was accompanied by another maximum at 188 mV; the two reduction maxima, having potentials at 358 and 188 mV, are characterized by current densities equal to 3.1 mA $cm^{-2}$ and 2.1 mA $cm^{-2}$, respectively. According to these results, regardless of the number of cyclic voltammograms recorded at the working electrode/electrolyte interface, two oxidation–reduction processes were evidenced by anode and cathode maxima having potentials located at (i) 430 mV and 364 mV and 246 mV and 186 mV, respectively, in the case of the first cyclic voltammogram; and (ii) 420 and 358 mV and 244 and 188 mV, respectively, in the case of the 50th cyclic voltammogram. All these variations were accompanied by a gradual increase in the density of the anode and cathode peaks. The two oxidation–reduction processes are characterized by $\Delta E$ equal to (i) 66 mV and 60 mV in the case of the first cyclic voltammogram, and (ii) 62 mV and 56 mV in the case of the 50th cyclic voltammogram. The ratio of the current densities of the anode and cathode peaks ($i_a/i_c$) is equal to (i) 0.87 and 0.68 in the case of the first cyclic voltammogram, and (ii) 0.93 and 0.76 in the case of the 50th cyclic voltammogram. These features indicate an improvement in the charge transfer kinetics and a partial enhancement of the reversibility of the redox

processes. These electrochemical differences can be directly correlated with the structural features identified in Section 3.1. Raman and XPS analyses demonstrated that electrochemical polymerization in the presence of RGO leads to covalent functionalization and a higher proportion of C–N bonds, along with modifications in the protonation state of the polymer chains. Unlike the composites obtained by simple mixing (where π–π interactions dominate), the electrochemically synthesized composites exhibit stronger electronic coupling between POT chains and RGO sheets. This structural configuration has two important consequences for the electrochemical response: (i) Enhanced electron transport as a result of the formation of covalent bonds and improved interfacial contact that reduces the resistance at the polymer/RGO interface, facilitating electron transfer during redox processes; this explains the higher current densities observed in Fig. 5b. (ii) Modified redox reversibility observed *via* the partial decrease in $\Delta E$ and the $i_a/i_c$ ratios closer to unity, suggesting faster charge transfer kinetics, which can be attributed to improved electronic delocalization and the presence of conductive pathways of RGO. However, the process remains quasi-irreversible due to structural heterogeneity and the coexistence of different oxidation states of the polymer, as shown by the spectroscopic data. At the end of the 50 cyclic voltammograms on the surface of the Pt electrode, the deposition of a dark green film corresponding to the POT/RGO composite was observed.

In order to confirm the formation of POT-ES and the POT-ES/RGO composite, Fig. 6 and 7 show the Raman and FTIR spectra of the two compounds.

According to Fig. 6a, the Raman spectrum of POT-ES is characterized by Raman lines with maxima located at 449, 1120, 1178, 1261, 1358, 1493, 1574 and 1624 $cm^{-1}$, which have been attributed by similarity to PANI to vibrational modes of aromatic ring deformation, $CH_3$ group deformation, C–H bending in the B ring, C–N stretching in the (B)–NH+=(Q), protonated structure, stretching C–C + C–H + N–H, N=(Q)=N stretching, and C–C stretching + C–H bending in the B ring.[22,23] Compared to Fig. 6a and b shows the following: (i) an up-shift in the Raman line from 449 $cm^{-1}$ (Fig. 6a) to 455 $cm^{-1}$ (Fig. 6b); (ii) a down-shift in the Raman line from 1120 $cm^{-1}$ (Fig. 6a) to 1115 $cm^{-1}$ (Fig. 6b), variation accompanied by a change in the ratio between the intensities of the Raman lines at 1120–1115 and 1178 $cm^{-1}$ from 1.89 to 0.81; (iii) the shift of Raman lines in the spectral range 1200–1400 $cm^{-1}$ from 1261 and 1358 $cm^{-1}$

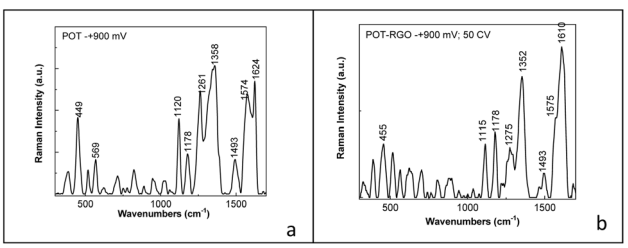


Fig. 6 Raman spectra of POT-ES (a) and the POT-ES/RGO composite (b) after recording the 50th cyclic voltammograms at a constant potential of 900 mV.

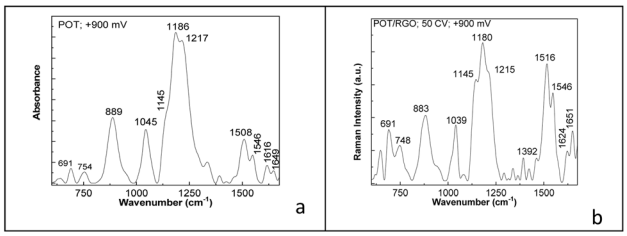


Fig. 7 FTIR spectra of POT (a) and the POT/RGO composite (b) after recording the 50 cyclic voltammograms at a constant potential of 900 mV.

(Fig. 6a) to 1275 and 1352 $cm^{-1}$ (Fig. 6b), simultaneously with an increase of the ratio between the intensities of the Raman lines from 1358–1352 and 1261–1275 $cm^{-1}$ from 1.25 (Fig. 6a) to 2.44 (Fig. 6b); and (iv) the shift of the Raman line from 1624 $cm^{-1}$ (Fig. 6a) to 1610 $cm^{-1}$ (Fig. 6b), which is accompanied by a variation of the ratio between the intensities of the Raman lines situated at 1575 and 1624–1610 $cm^{-1}$ from 0.88 (Fig. 6a) to 0.53 (Fig. 6b). This change suggests a diminution of the share of the N=Q=N structure, which can be explained as a consequence of the transformation of the Q ring into the B ring when covalent functionalization of the RGO sheets with POT-ES occurs.

Fig. 7a shows the FTIR spectrum of POT-ES, which is characterized by IR bands located at 691, 754, 889, 1045, 1145, 1185, 1217, 1508, 1616, and 1651 $cm^{-1}$, attributed to vibrational modes of B ring deformation, Q ring deformation, out-of-plane deformation of the three-substituted B ring, deformation of C–$CH_3$, bending of C–H in-plane in N=Q=N, Q=$NH^+$–B and B–$NH^+$–B structures, $C_{aromatic\ ring}$–N stretching, stretching in N–B–N, stretching of the N=Q=N structure, and C=C stretching.[29–32] Compared to Fig. 7a, the following changes were observed in Fig. 7b: (i) an increase in the absorbance of IR bands with maxima at 691 $cm^{-1}$ (Fig. 7a) and 748 $cm^{-1}$ (Fig. 7b); (ii) a down-shift of the IR bands from 889 and 1045 $cm^{-1}$ (Fig. 7a) to 883 and 1039 $cm^{-1}$ (Fig. 7b); (iii) an up-shift of the IR band from 1508 $cm^{-1}$ (Fig. 7a) to 1516 $cm^{-1}$ (Fig. 7b) simultaneously with an increase in its absorbance; (iv) changing the ratio between the absorbances of the IR band located in the spectral ranges 1100–1250, 1500–1575 and 1600–1700 $cm^{-1}$ ($A_{1100-1250}/A_{1500-1575}$ and $A_{1100-1250}/A_{1600-1700}$) from 3.42 and 5.54 (Fig. 7a) to 1.16 and 1.66 (Fig. 7b). These variations clearly indicate a decrease in the proportion of the Q=$NH^+$–B and B–$NH^+$–B structures in contrast to the N–B–N and N=Q=N structures, when electrochemical polymerization of OT in the presence of RGO sheets takes place. An explanation for this variation must take into account the mechanism of the electrochemical polymerization of OT in the presence of RGO, which is shown in Scheme 1S. The mechanism of the electrochemical polymerization of OT in the presence of RGO involves the following: (i) an oxidation reaction of OT, when the cationic radical of OT results; (ii) the chemical interaction of the radical cation of OT with the RGO sheets, when a covalent functionalization of RGO with OT takes place; (iii) the macromolecular chain propagation reaction of POT when the reaction product

corresponds to POT-LS-functionalized RGO sheets, followed by its transformation into POT-ES-functionalized RGO sheets.

Fig. 8 shows the XPS C 1s, N 1s, and O 1s spectra of POT-ES and the POT-ES/RGO composite prepared by the electrochemical method. The XPS C 1s spectrum of POT-ES (Fig. 8a) presents by deconvolution four bands with maxima at 284.3, 285, 285.7, and 286.6 eV, which were assigned to the C–C/C–H, C–N/C=N, C–$N^+$/C=$N^+$, and C=O/C–O bonds, respectively.[33] The deconvolution of the XPS N 1s spectrum of the POT-ES (Fig. 8c) illustrates three bands with maxima at 399.3, 400.8, and 402.2 eV, which were assigned to bonds C–N=C,[30] C–NH–C,[28] and C–$N^+$, respectively.[33] The deconvolution of the XPS O 1s spectrum of POT-ES (Fig. 8e) illustrates three bands with maxima at 531.4, 532.8, and 533.9 eV, which have been assigned to the C=O, S–O/C–O, and O–H bonds.[33]

Analysis of the XPS C 1s spectrum of the POT/RGO composite shows that with deconvolution, four bands can be observed at 284.3, 285, 285.7, and 286.6 eV (Fig. 8b). A comparative analysis of the XPS C 1s spectra of POT (Fig. 8a) and the POT/RGO composite (Fig. 8b) revealed that the ratio of the intensities of the four bands is 1 : 0.27 : 0.16 : 0.1 (Fig. 8a) and 1 : 0.34 : 0.09 : 0.08 (Fig. 8b). This indicates a smaller proportion of C–$N^+$/C=$N^+$ bonds concomitant with an increase in the proportion of C–N/C=N bonds in the POT-ES/RGO composite compared to POT-ES. This result confirms the mechanism proposed in Scheme 1S, where the formation of new covalent bonds of the type C–N onto the surface of RGO sheets is reported. Fig. 8d shows the deconvolution of the XPS N 1s spectrum of the POT/RGO composite, when only two bands with maxima at 399.3 and 401 eV, assigned to the C–N=C and C–NH–C bonds, are observed.[28] The deconvolution of the XPS O 1 s spectrum of the POT/RGO composite (Fig. 8f) shows three bands located at 531.5, 532.8, and 534 eV that were assigned to the C=O, S–O/C–O, and O–H bonds.[33] The ratio of the intensities of the bands assigned to C=O and S–O bonds is 1 : 0.6 for both POT-ES and the POT-ES/RGO composite, which indicates similar repeating units in the two compounds. The spectroscopic and electrochemical results demonstrate that electrochemical polymerization in the presence of RGO leads to a structurally integrated composite, in which covalent bonds and enhanced electronic coupling enhance charge transport while maintaining a quasi-reversible redox behavior. This provides a direct link between the molecular structure of the composite and its electrochemical response, addressing the role of RGO in modulating both conductivity and redox activity.

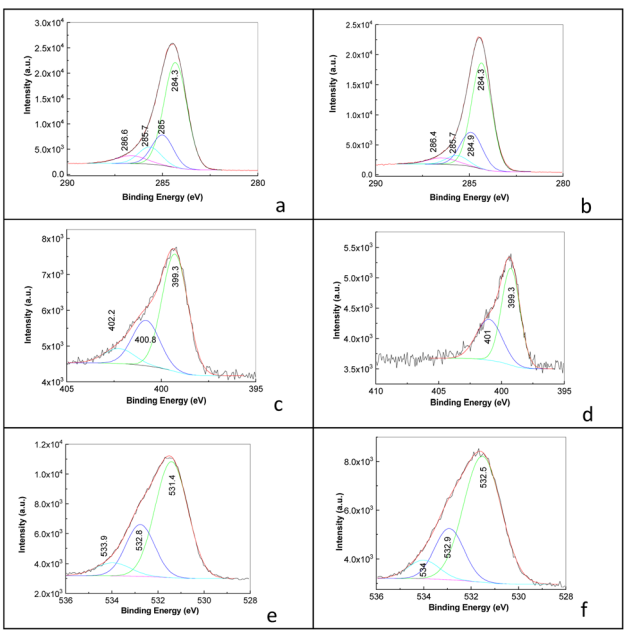


Fig. 8 XPS spectra of POT-ES and the POT/RGO composites obtained by the electrochemical polymerization of OT in the presence of RGO sheets: C 1s (a, and b), N 1s (c, and d), and O 1s (e, and f).

### 3.3 Preliminary studies of the electrochemical properties of the POT/RGO composites as promising active electrode materials in symmetrical supercapacitor cells

Fig. 9 shows cyclic voltammograms of POT-EB, the POT/RGO composites prepared by the interaction of the two constituents, and chemical and electrochemical polymerization of OT in the presence of RGO, when a membrane of Nafion activated with 1 M $H_2SO_4$ as electrolyte was used.

A careful analysis of Fig. 9 highlights that the voltammetric output currents of the composites prepared by the three methods are superior to those reported for POT-EB. This is due to the large surface area of RGO and improved electrical conductivity at the electrode/electrolyte interface. However, the magnitude of this improvement strongly depends on the synthesis method, reflecting the structural differences evidenced by Raman, FTIR, and XPS analyses. Current densities have two components: one is related to the double-layer charge at the electrode/electrolyte interface, and the other is induced by the intercalation processes, which are controlled by diffusion. The contribution of the two processes, *i.e.*, capacitive and diffusion, can be determined using the following equation: $i(V) = a \times v^b$, where $i$ and $v$ correspond to current density (A $cm^{-2}$) and potential scan rate (mV $s^{-1}$), while $a$ and $b$ are two constants.[34] Depending on the value of $b$, estimated from the slope of the plot of $\log(i)$ *vs.* $\log(v)$, the electrode material shows the following: (a) $b = 1$, a redox reaction at the electrode surface and the charge/discharge processes of the electric double-layer capacitors (EDLC); (b) $0.8 < b < 1$, pseudocapacitive behavior; (c) $0.5 < b < 0.8$, battery-type behavior.[34] The results shown in Fig. 9g and h demonstrate clearly that (a) the electrodes based on POT-EB, POT-ES, and POT/RGO prepared by chemical and electrochemical polymerization of OT in the presence of RGO sheets have a battery-type behavior, indicating that charge storage is dominated by diffusion-controlled intercalation processes; (b) electrodes having active material composites resulting from the interaction in the solid state of the two constituents, *i.e.*, POT-EB and RGO, show pseudocapacitive behavior. This difference can be directly correlated with the structural features identified earlier: the weak π–π interactions in solid-state composites favor surface-controlled processes, whereas the stronger coupling and partial protonation observed

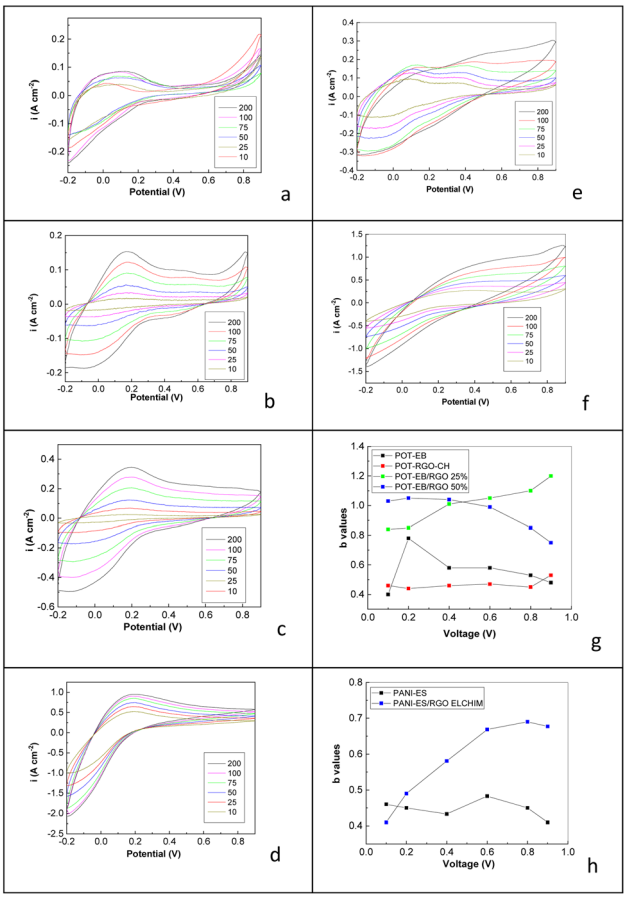


Fig. 9 5th cyclic voltammogram of POT-EB (a), POT-EB/RGO composites obtained by the solid-state interactions of the two constituents, with RGO concentrations of 25 wt% (b) and 50 wt% (c) as well as by the chemical polymerization of OT in the presence of RGO at an RGO concentration of 20 wt% (d); POT-ES (e), and the POT-ES/RGO composite (f) synthesized by the electrochemical polymerization of OT in the presence of RGO. Black, red, green, blue, magenta, and dark yellow in figure a–f correspond to the cyclic voltammograms recorded at the scan rates of 200, 100, 75, 50, 25, and 10 mV $s^{-1}$, respectively. Figure (g) and (h) show dependence of the *b*-value on voltage in the case of the supercapacitors having electrode materials of POT-EB and POT-EB/RGO composites synthesized by solid state interactions and chemical polymerization as well as POT-ES and the POT-ES/RGO composite synthesized by the electrochemical polymerization of OT in the presence of the RGO sheets, respectively.

in chemically/electrochemically synthesized materials promote bulk redox activity.

In order to assess the contribution of the surface capacitive process and the process of intercalation, which is controlled by diffusion, in the cyclic voltammograms, the protocol described in ref. 34–36 is used. Briefly, this uses the equation $i(V) = k_1\nu + k_2\nu^{1/2}$, where $i(V)$ is the current density at a fixed potential, while $k_1\nu$ and $k_2\nu^{1/2}$ correspond to the weight of the capacitive effect and the intercalation process. The values of $k_1$ and $k_2$ are determined from the linear fitting of the dependence $i(V)/\nu^{1/2}$ *vs.* $\nu^{1/2}$.

The analysis of Fig. 10 and 11 indicates that electrodes containing the active materials POT-EB and the POT/RGO composite, with an RGO concentration equal to 20 wt%, prepared by chemical polymerization of OT in the presence of RGO, have a significant contribution from diffusion-controlled intercalation processes, consistent with the presence of protonated POT-ES structures and enhanced ion insertion within the bulk material. This behavior is in agreement with FTIR and Raman results, which indicated increased structural reorganization and a higher density of redox-active sites. The increase in the RGO concentration in the POT-EB/RGO composite mass, prepared by the interaction in the solid state of the two constituents, leads to an increase in the capacitance of the symmetrical supercapacitors. In contrast to POT-ES, the presence of RGO in the composite prepared by the electrochemical polymerization of OT leads to an increase in the contribution of capacitive processes compared with that of diffusion-controlled intercalation processes. The reactions that take place at the electrode/electrolyte interface are shown in Scheme 2S.

Fig. 12 shows the dependence of capacitance on the potential scan rate of the electrodes prepared in this study. A decrease in capacitance as the potential scan rate increases occurs in all cases. At the same potential scan rate, *e.g.* 10 mV $s^{-1}$, the capacitance of PANI-EB and the composites obtained by the solid-state interactions of the two constituents having the

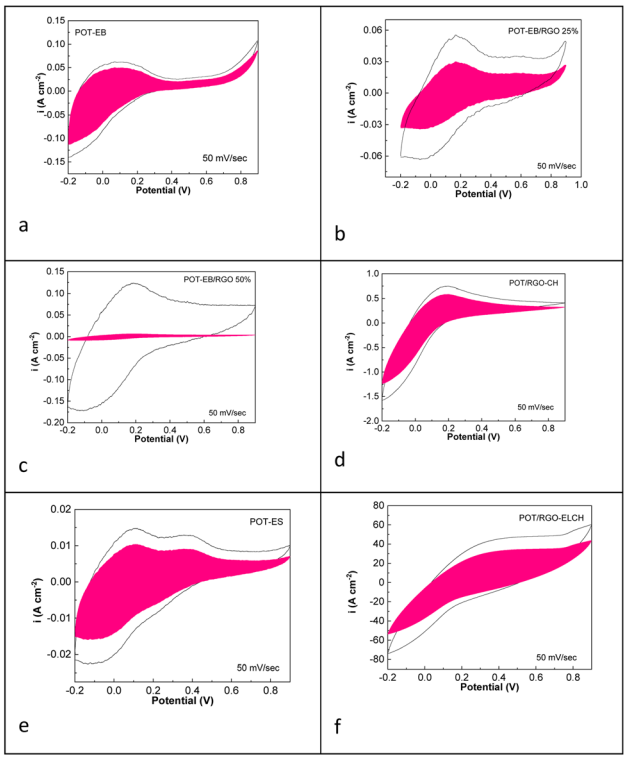


Fig. 10 Deconvoluted intercalation (pink area) and capacitance (white area) of POT-EB (a), the POT-EB/RGO composites with RGO concentrations of 25 wt% (b) and 50 wt% (c) obtained by interactions in the solid state; the POT/RGO composite obtained by the chemical polymerization of OT in the presence of the RGO (d), the RGO concentration in the composite was 20 wt%), POT-ES (e), and the POT-ES/RGO composite obtained by the electrochemical polymerization of OT in the presence of the RGO sheets (f).

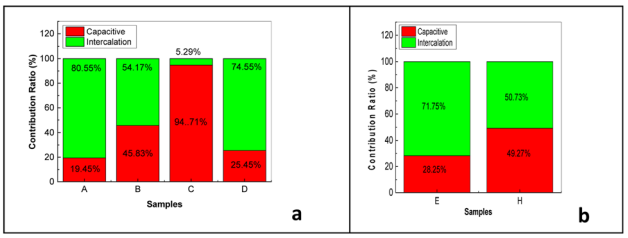


Fig. 11 Contribution ratios between capacitive and diffusive processes for the samples of (a) POT-EB (sample A), the POT/RGO composites with an RGO concentration equal to 25 wt% (sample B) and 50 wt% (sample C), the POT-EB/RGO composite synthesized by the chemical polymerization of OT in the presence of the RGO sheets with an RGO concentration of 20 wt% (sample D) and (b) POT-ES (sample E) and the POT-ES/RGO composite synthesized by the electrochemical method (sample H).

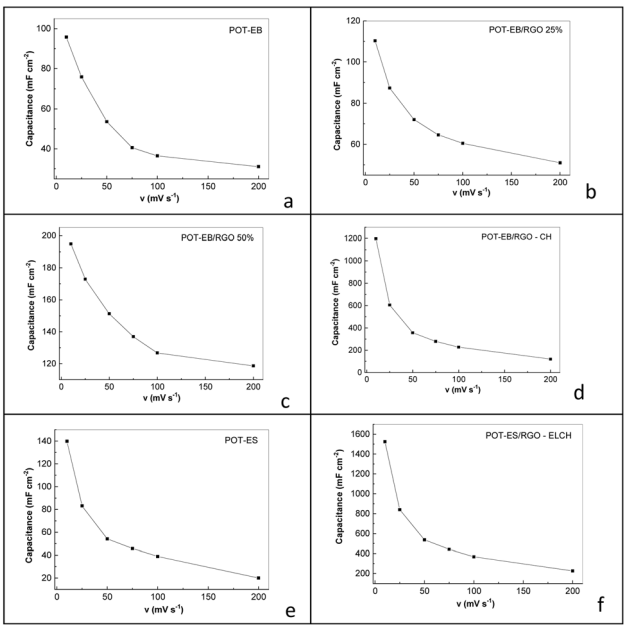


Fig. 12 Dependence of capacitance on the potential scan rate of electrodes based on (a) POT-EB, (b) the POT-EB/RGO composite, prepared by the interaction of the two constituents in the solid state, when the RGO concentration was 25 wt%, (c) the POT-EB/RGO composite, resulting from the solid-state interactions of the constituents with an RGO concentration of 50 wt%, (d) the POT-EB/RGO composite synthesized by the chemical polymerization of OT in the presence of RGO sheets, with the RGO concentration in the composite mass being 20 wt%, (e) POT-ES, and (f) the POT-ES/RGO composite synthesized by the electrochemical polymerization of OT in the presence of RGO.

concentration of RGO equal to 25 wt% and 50 wt% in the composite mass and the POT/RGO composite synthetized by the chemical polymerization of OT in the presence of RGO sheets varied from 95.82 mF $cm^{-2}$ (Fig. 12a) to 110.31 mF $cm^{-2}$ (Fig. 12b), 194.98 mF $cm^{-2}$ (Fig. 12c) and 1197.23 mF $cm^{-2}$ (Fig. 12d), respectively. In the case of the supercapacitors based on electrodes containing POT-ES and the POT-ES/RGO composite as active materials, compounds synthesized by the electrochemical polymerization of OT in the absence and in the presence of RGO sheets, the capacitance varied from 139.88 mF $cm^{-2}$ (Fig. 12e) to 1524.62 mF $cm^{-2}$ (Fig. 12f) when the potential scan rate was of 10 mV $s^{-1}$. The significantly higher capacitance of composites obtained by chemical and electrochemical polymerization (Fig. 12d and f) can be attributed to the combined effects of (i) increased electrical conductivity due to enhanced conjugation (as shown by Raman scattering), (ii) higher density of redox-active sites associated with protonated POT-ES structures (as highlighted by FTIR spectroscopy and XPS), and (iii) improved electrode/electrolyte interface provided by RGO sheets. In the case of the electrochemically synthesized composites, the covalent functionalization of RGO with POT leads to a more efficient electronic coupling, which explains the highest capacitance values observed. The increased contribution of capacitive processes in these materials indicates improved surface accessibility, consistent with the structural modifications evidenced by Raman and FTIR spectroscopy.

Fig. 13 shows the dependence of the capacitance of the supercapacitors having electrodes based on POT-EB, POT-ES, the POT-EB/RGO composites prepared by the interaction of the two constituents, when the RGO concentration was equal to 50 wt%, the POT-EB/RGO composite chemically synthesized with a RGO concentration equal to 20%, POT-ES, and the POT-ES/RGO composite electrochemically synthesized with the cyclic

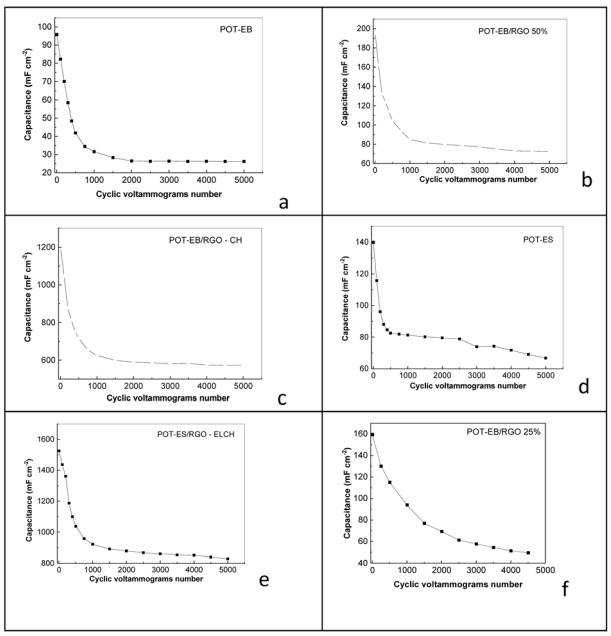


Fig. 13 Dependence of capacitance on the number of cyclic voltammograms recorded at a potential scan rate of 200 mV $s^{-1}$ in the case of electrodes based on (a) POT-EB, (b) the POT-EB/RGO composite prepared by the interaction of the two constituents with an RGO concentration equal to 50 wt%, (c) the POT-EB/RGO composite synthesized by the chemical polymerization of OT in the presence of RGO sheets with an RGO concentration in the composite mass equal to 20 wt%, (d) POT-ES, (e) the POT-ES/RGO composite synthesized by the electrochemical polymerization of OT in the presence of RGO and (f) the POT-EB/RGO composite prepared by the interaction of the two constituents with an RGO concentration equal to 25 wt%.

voltammogram numbers, recorded when the potential scan rate was equal to 20 mV $s^{-1}$. According to Fig. 13, a significant decrease in the capacitance takes place in all cases in the first 1000 cyclic voltammograms. At the end of the 5000 cyclic voltammograms, the capacitance values of the electrodes having the active materials of POT-EB and the POT/RGO composites obtained by the interaction in the solid state of the two constituents, chemical polymerization and electrochemical polymerization, respectively, of OT in the presence of RGO were 26.2 mF $cm^{-2}$ (Fig. 13a), 48.6 mF $cm^{-2}$ (Fig. 13f), 66.75 mF $cm^{-2}$ (Fig. 13d), 72.66 mF $cm^{-2}$ (Fig. 13b), 573.53 mF $cm^{-2}$ (Fig. 13c) and 828.96 mF $cm^{-2}$ (Fig. 13e). Materials obtained by electrochemical polymerization exhibited significantly higher residual capacitance than POT-EB and the solid-state composites. This improved stability can be attributed to the stronger interfacial bonding between POT and RGO, which prevents structural degradation during repeated charge/discharge cycles. The weaker interactions in solid-state composites lead to poorer mechanical and electrochemical stability.

These preliminary results demonstrate that the electrochemical performance of the POT/RGO composites is governed not only by the presence of RGO but, more importantly, by the nature of the interactions between the polymer and RGO. Strong electronic coupling, partial protonation, and covalent functionalization collectively lead to enhanced charge transport, increased redox activity, and improved capacitive performance.

## 4 Conclusions

Herein, we have reported new results from our investigation on the influence of the synthesis route on the structural and electrochemical properties of the POT/RGO composites, and we aimed to identify the key parameters governing their performance as electrode materials for supercapacitors. The results obtained from Raman scattering, FTIR spectroscopy, X-ray photoelectron spectroscopy, and cyclic voltammetry demonstrate that the electrochemical behavior of these materials is strongly dependent on the nature of the interaction between POT and RGO. While the solid-state interaction of POT with RGO leads to weak π–π coupling and predominantly pseudocapacitive behavior, the chemical and electrochemical polymerization of OT in the presence of RGO promotes partial protonation of the polymer (POT-ES), increased C–N bonding, and stronger electronic coupling with RGO sheets. These structural features directly enhance charge transport, increase the density of redox-active sites, and improve electrolyte accessibility, resulting in significantly higher capacitance values and improved electrochemical performance. In particular, the POT-ES/RGO composites obtained by electrochemical polymerization exhibit the best performance (having a capacitance value of 828.96 mF $cm^{-2}$) due to the formation of covalent bonds and an optimized interface structure. Electrodes based on POT EB, POT ES, and the chemically or electrochemically synthesized POT/RGO composites exhibit battery-type behavior, whereas composites obtained by solid-state interaction show pseudocapacitive characteristics.

This study has highlighted that the optimization of the polymer–carbon interface, rather than simply increasing the RGO content, is the key factor in designing high-performance electrode materials. These findings provide useful guidelines for the development of advanced conducting polymer-based composites for energy storage applications. Future work will focus on improving the long-term cycling stability, exploring scalable synthesis strategies, and the use of composite materials in asymmetric supercapacitor cells.

## Conflicts of interest

The authors have no known competing financial interests or personal relationships that could have appeared to influence this manuscript. There are no conflicts to declare.

## Data availability

The data that support the findings of this study are available from the corresponding author upon reasonable request.

Supplementary information (SI) is available. See DOI: https://doi.org/10.1039/d6ra00288a.

## Acknowledgements

This work is funded by the Core Program of the National Institute of Materials Physics, granted by the Romanian Ministry of Research, Innovation, and Digitization through the Project PC3-PN23080303.

## References

1 S. W. Feldberg, Reinterpretation of polypyrrole electrochemistry. Consideration of capacitive currents in redox switching of conducting polymers, *J. Am. Chem. Soc.*, 1984, **106**, 4671–4674, DOI: 10.1021/ja00329a004.

2 Y. Liang, Z. Wei, E. H. Wang, R. Wang and x. Zhang, Flexible freestanding conductive nanopaper based on PPy:PSS nanocellulose composite for supercapacitors with high performance, *Sci. China Mater.*, 2023, **66**, 964–973, DOI: 10.1007/s40843-022-2225-x.

3 E. Dhandapani, S. Thangarasu, S. Ramesh, K. Ramesh, R. Vasudevan and N. Duraisamy, Recent development and perspective of carbonaceous materials, conducting polymers and their composite electrode materials for supercapacitor – A review, *J. Energy Storage*, 2022, **52**, 104937, DOI: 10.1016/j.est.2022.104937.

4 M. Zhang, A. Nautiyal, H. Du, Z. Wei, X. Zhang and R. Wang, Electropolymerization of polyaniline as high-performance binder free electrodes for flexible supercapacitors, *Electrochim. Acta*, 2021, **376**, 138037, DOI: 10.1016/j.electacta.2021.138037.

5 A. Moysevwicz, D. Minta and G. Gryglevicz, Conductive polymer/graphene-based composites for next generation energy storage and sensing applications, Chem. Electro, *Chem*, 2023, **10**, e202201145, DOI: 10.1002/celc.202201145.

6 C. I. Idumah, A review on polyaniline and graphene nanocomposites for supercapacitors, *Polym.-Plast. Technol. Mater.*, 2022, **61**, 1871–1907, DOI: 10.1080/25740881.2022.2086810.
7 V. Meriga, S. Valligatta, S. Sundaresan, C. Cahill, V. R. Dhanak and A. K. Chakraborty, Optical, electrical, and electrochemical properties of graphene based water soluble polyaniline composites, *J. Appl. Polym. Sci.*, 2015, **132**, 42766, DOI: 10.1002/app.42766.
8 N. Chen, Y. Ren, P. Long, L. Tan, H. Feng and Y. Luo, In situ one-pot preparation of reduced graphene oxide/polyaniline composite for high-performance electrochemical capacitors, *Appl. Surf. Sci.*, 2017, **392**, 71–79, DOI: 10.1016/j.apsusc.2016.07.168.
9 Y. Li and Y. Zheng, Preparation and electrochemical properties of polyaniline/reduced graphene oxide composites, *J. Appl. Polym. Sci.*, 2018, **135**, 46103, DOI: 10.1002/app.46103.
10 J. C. Gabunada, M. Vinothkannan, D. H. Kim, A. R. Kim and D. J. Yoo, Magnetite nanorods stabilized by polyaniline/graphene oxide as a sensing platform for selective and sensitive non-enzymatic hydrogen peroxide detection, *Electroanalytical*, 2019, **31**, 1507–1516, DOI: 10.1002/elan.201900134.
11 S. Mondal, U. Rena and S. Malik, Reduced graphene oxide/Fe3O4/Polyaniline nanostructures as electrode materials for all-solid-state hybrid supercapacitor, *J. Phys. Chem. C*, 2013, **121**, 7573–7583, DOI: 10.1021/acs.jpcc.6b10978.
12 D. A. L. Almeida, A. B. Couto and N. G. Ferreira, Flexible polyaniline/reduced graphene oxide/carbon fiber composites applied as electrodes for supercapacitors, *J. Alloys Compd.*, 2019, **788**, 453–460, DOI: 10.1016/j.jallcom.2019.02.194.
13 P. A. Basnayaka, M. K. Ram, L. Stefanakos and A. Kumar, High performance graphene-poly(o-anisidine) nanocomposite for supercapacitor applications, *Mater. Chem. Phys.*, 2013, **141**, 263–271, DOI: 10.1016/j.matchemphys.2013.05.009.
14 M. Baibarac, L. Mihut, G. Louarn, S. Lefrant and I. Baltog, Doping and metallic-support effect evidenced on SERS spectra of polyaniline thin films, *J. Polym. Sci., Part B*, 2000, **38**, 2599–2609, DOI: 10.1002/1099-0488(20001001)38:19%3C2599:AID-POLB120%3E3.0.CO;2-Y.
15 M. Lapkowski, K. Berrada, S. Quillard, G. Louarn, S. Lefrant and A. Pron, Electrochemical oxidation of polyaniline in nonaqueous electrolytes "in situ" Raman spectroscopic studies, *Macromolecules*, 1995, **28**, 1233–1238, DOI: 10.1021/ma00108a061.
16 M. R. Saeb, P. Zarrintak, P. Khandelwal, and N. P. S. C. Chauhar, Synthetic route of polyaniline (I): Conventional oxidative polymerization, in *Fundamentals and Emerging Applications of Polyaniline*, ed. M. Mozafari, and N. P. S. Chauhan, Elsevier, 2019, pp. 17–41. DOI: 10.1016/B978-0-12-817915-4.00002-6.
17 D. C. Marcano, D. V. Kosynkin, J. M. Berlin, A. Sinitskii, Z. Sun, A. Slesarev, L. B. Alemany, W. Lee and J. M. Tour, Improved synthesis of graphene oxide, *ACS Nano*, 2010, **4**, 4806–4814, DOI: 10.1021/nn1006368.
18 T. Burlanescu, I. Smaranda, A. Androne, C. S. Florica, M. Cercel, M. Paraschiv, A. Udrescu, A. Lorinczi, P. Palade, A. Galatanu, c. Negrila, E. Matei, M. Dinescu, R. Cercel and M. Baibarac, Composites based on poly(ortho-toluidine) and $WS_2$ sheets for applications in the supercapacitors field, *Batteries*, 2025, **11**, 37, DOI: 10.3390/batteries11010037.
19 M. Baibarac, I. Baltog, S. Frunza, A. Magrez, D. schur and S. Yu Zaginaichenko, Single-walled carbon nanotubes functionalized with polydiphenylamine as active materials for applications in the supercapacitors field, *Diam. Relat. Mater.*, 2013, **32**, 72–82, DOI: 10.1016/j.diamond.2012.12.006.
20 R. Kuwertz, C. Kirstein, T. Turek and U. Kunz, Influence of acid pretreatment on ionic conductivity of Nafion membranes, *J. Membr. Sci.*, 2016, **500**, 225–235, DOI: 10.1016/j.memsci.2015.11.022.
21 P. M. Luc, F. Buchwald and J. Kowal, Reproducibility of small-format laboratory cells, *Energies*, 2022, **15**, 7333, DOI: 10.3390/en15197333.
22 S. Quillard, G. Louarn and S. Lefrant, Vibrational analysis of polyaniline: a comparative study of leucoemeraldine, emeraldine and pernigraniline bases, *Phys. Rev. B:Condens. Matter Mater. Phys.*, 1994, **50**, 12496, DOI: 10.1103/PhysRevB.50.12496.
23 R. D. Bowen, H. G. M. Edwards and T. Varnali, Influence of a methyl substituent on the Raman spectrum of butyl 3-methyl ether, *Spectrochim. Acta, Part A*, 2012, **93**, 26–32, DOI: 10.1016/j.saa.2012.02.059.
24 S. Eigler, C. Dotzer and A. Hirsch, Visualization of defect densities in reduced graphene oxide, *Carbon*, 2002, **50**, 3666–3673, DOI: 10.1016/j.carbon.2012.03.039.
25 Y. Liang, Z. Wei, H. E. Wang, M. Flores, R. Waang and X. Zhang, Flexible and freestanding PANI:PSS/CNF nanopaper electrodes with enhanced electrochemical performance for supercapacitors, *J. Power Sources*, 2022, **548**, 232071, DOI: 10.1016/j.jpowsour.2022.232071.
26 C. Xu, X. Shi, A. Ji, L. Shi, C. Zhou and Y. Cui, Fabrication and characteristics of reduced graphene oxide produced with different green reductants, *PLoS One*, 2015, **10**, e0144842, DOI: 10.1371/journal.pone.0144842.
27 S. Golczak, A. Kanciurzewska, M. Fahlman, K. Langer and J. J. Langer, Comparative XPS surface study of polyaniline thin films, *Solid State Ionics*, 2008, **179**, 2234–2239, DOI: 10.1016/j.ssi.2008.08.004.
28 M. M. Mahat, D. Mawad, G. W. Nelson, S. Fearn, R. G. Palgrave, D. J. Payne and M. M. Stevens, Elucidating the deprotonation of polyaniline films by X-ray photoelectron spectroscopy, *J. Mater. Chem. C*, 2015, **3**, 7180–7186, DOI: 10.1039/c5tc01038a.
29 M. Trchova, I. Stejskal and J. Prokes, Infrared spectroscopic study of solid-state protonation and oxidation of polyaniline, *Synth. Met.*, 1999, **101**, 840–841, DOI: 10.1016/S0379-6779(98)01310-1.
30 Z. Ping, G. Nauer, H. Neugebauer, J. Theiner and A. Neckel, Protonation and electrochemical redox doping processes of

polyaniline in aqueous solutions: investigations using in-situ FTIR-ATR spectroscopy and a new doping system, *J. Chem. Soc., Faraday Trans.*, 1997, **93**, 121–129, DOI: 10.1039/a604620g.

31 E. M. Andrache, F. V. Molina, M. I. Florit and D. Posadas, IR response of poly(o-toluidine): spectral modifications upon redox state change, *J. Electroanal. Chem.*, 1996, **419**, 15–21, DOI: 10.1016/S0022-0728(96)04874-7.

32 W. S. Sugianto, D. Nitami and S. M. Ulfa, Facile synthesis of lycopene reduced graphene oxide in different solvent polarity, *IOP Conf. Ser.:Mater. Sci. Eng.*, 2019, **546**, 042044, DOI: 10.1088/1757-899X/546/4/042044.

33 M. S. Wu, T. C. Wen and A. Gopalan, Electrochemical co-polymerization of diphenylamine and anthranilic acid with various feed ratios, *J. Electrochem. Soc.*, 2001, **148**, D65, DOI: 10.1149/1.1366625.

34 W. H. Cho, I. C. Cheng and J. Z. Chen, Performance comparison of reduced graphene oxide (rGO)-polyaniline (PANI) supercapacitors with LiCl, $Li_2SO_4$, and $H_2SO_4$ electrolyte, *J. Electrochem. Soc.*, 2023, **170**, 010532, DOI: 10.1149/1945-7111/acb38b.

35 M. Zhang, H. di, Z. Wei, X. Zhang and R. Wang, Facile electrodeposition of Mn-CoP nanosheets on Ni foam as high-rate and ultrastable electrodes for supercapacitors, *ACS Appl. Energy Mater.*, 2022, **5**, 186–195, DOI: 10.1021/acsaem.1c02730.

36 M. Zhang, H. Du, Z. Wei, X. Zhang and R. Wang, Ultrafast microwave synthesis of nickel-cobolt sulfide/graphene hybrid electrodes for high-performance asymmetrical supercapacitors, *ACS Appl. Energy Mater.*, 2021, **4**, 8262–8274, DOI: 10.1021/acsaem.1c01507.